The formation of planar crystalline flocs of γ-FeOOH in Fe(II) coagulation and the influence of humic acid

Xian Li [a,b], Nigel J. D. Graham [c], Wensheng Deng [a], Mengjie Liu [b], Ting Liu [a*], and Wenzheng Yu [b *]

[a] *School of Chemistry and Chemical Engineering, Beijing Institute of Technology, Beijing 100081, China (liuting@bit.edu.cn)*

[b] *State Key Laboratory of Environmental Aquatic Chemistry, Key Laboratory of Drinking Water Science and Technology, Research Center for Eco-Environmental Sciences, Chinese Academy of Sciences, Beijing 100085, People's Republic of China.*

(wzyu@rcees.ac.cn)

[c] *Department of Civil and Environmental Engineering, Imperial College London, South Kensington Campus, London SW7 2AZ, UK.*

Abstract

Although Fe(II) salts have been widely used as coagulants in water treatment for many years, the underlying mechanisms of their performance remain unclear. Here, we present a detailed study of the coagulation behavior of Fe(II) salts and crystallization of flocs, and investigate the effect of humic acid (HA) under different DO concentrations and pH conditions. The behavior of Fe(II) and Fe(III) coagulants was found to be markedly different with the flocs from Fe(II) consisting of planar-like crystalline γ-FeOOH in contrast to the small amorphous spherical-like flocs from

Fe(III) dosing. The effect of HA on Fe(II) coagulation was different under different DO concentrations and pH, whereby the growth of γ-FeOOH was inhibited by the presence of HA, but independent of DO concentration and pH. It was found that Fe(II) was present within the internal structure of γ-FeOOH, and a plausible formation mechanism is proposed. Firstly, planar nanoparticles of $Fe(OH)_2$ were formed via Fe(II) ion hydrolysis which then served as the nucleus for subsequent crystal growth. With oxidation, Fe(II) on the surface of nanoparticles transformed to Fe(III). Finally, the formation of γ-FeOOH in Fe(II) coagulation was accompanied by a change in solution colour to yellow.

Keywords: Fe(II) coagulation; planar-like flocs; crystalline γ-FeOOH; HA; DO; pH

1. Introduction

Iron (Fe) exists ubiquitously in the earth's crust, and is of major scientific and industrial importance (Cornell et al., 2003). Fe (hydr)oxides are an important factor in many anthropogenic and natural processes including environmental remediation, biogeochemical cycling of metals and interactions with natural organic matter (Gaffney et al., 2008; Okamura et al., 2016; Tagliabue et al., 2017; Yang et al., 2016). In addition, owing to their large surface area and variable redox state, Fe (hydr)oxides have been extensively studied in diverse fields, including water treatment, catalysis and storage media (Ellis et al., 2010; Okamura et al., 2016; Shekhah et al., 2003).

Coagulation is a common process in conventional water treatment, and Fe salts, as well as aluminium salts, are widely used as coagulants (Wu et al., 2019). Compared with aluminum salts, Fe salts can be used as a coagulant over a wider range of pH and temperature, and have been found to produce larger flocs which settle more easily (Hsu, 1976). Among Fe coagulants, ferrous (Fe(II)) salts are cheaper than ferric (Fe(III)) salts, but require conversion to Fe(III) for effective coagulation. It is generally believed that in-situ-formed Fe(III) species, via Fe(II) oxidation with oxidant chemicals such as H_2O_2, $KMnO_4$, ozone, or O_2, are generally more effective in water treatment than directly adding Fe(III) salts (Liu et al., 2017; Liu et al., 2018; Ma et al., 2012; Zhang et al., 2019; Zhou et al., 2019). It is well known that hydrolyzed Fe nano-precipitates form rapidly and then aggregate after Fe(II)/Fe(III) salts are added to water at around neutral or alkaline pH (Duan et al., 2003). In recent years, the influence of different coagulation variables (such as the type and concentration of coagulant), as well as the characteristics (such as strength and re-growth ability) of flocs, have received considerable attention (Xu et al., 2010; Yu et al., 2010; Yu et al., 2011; Yu et al., 2015). These studies have indicated that the majority of fresh flocs formed by coagulation are composed of thousands of primary spherical nanoparticles (Su et al., 2017; Wu et al., 2019), and that with aging some crystallization of nanoparticles occurs and changes in their structures occur (Yu et al., 2016a; Yu et al., 2018). In addition, it was found that organic matter, such as humic-like substances which exist ubiquitously in surface water, can affect the

aggregation between nanoparticles (Bian et al., 2011; Jarvis et al., 2005), and the crystallization and transformation of Fe (hydr)oxides (Xing et al., 2020).

In the past, much effort has been made to explore the crystallization and transformation of Fe (hydr)oxides, because the mobility of a wide range of contaminants is highly dependent on the crystallization or transformation of Fe products (Boland et al., 2014; Shu et al., 2019). The crystallization phase is generally explained in terms of two distinct growth modes: the ‘Ostwald ripening mode’, in which nanoparticles grow larger at the expense of small ones, and the ‘Oriented attachment mode’, in which nearby nanoparticles with pre-aligned crystallographic orientations aggregate into a single particle (De Yoreo et al., 2015; Ostwald, 1897; Zhang et al., 2017; Zhu et al., 2018). Various Fe (hydr)oxides with different crystal structures, such as urchin-like forms, rods, nanowires, tubes, porous spheres and flakes have been successfully found under different conditions (Hu et al., 2008; Liu et al., 2013; Matamoros-Veloza et al., 2018; Meng et al., 2011; Sayed et al., 2015; Yang et al., 2004; Zhong et al., 2006). However, these structures only occur with specific organic matter at certain temperatures and pressures, which may have little relevance to the crystallization of flocs during coagulation.

Previous research has revealed some factors that affect the coagulation performance of Fe salts and the crystallization process of Fe (hydr)oxides (Chorghe et al., 2017; Liu et al., 2013); however, few studies have focused on the crystallization of flocs during coagulation by Fe salts, and especially Fe(II) salts. The objective of the

research presented in this study was to investigate the Fe(II) coagulation and crystallization of flocs, and the effect of humic acid (HA) under different dissolved oxygen (DO) concentrations and pH conditions. The HA represents a major fraction of the dissolved organic matter in source waters, which was considered previously as a factor affecting the Fe(II) coagulation and crystallization of flocs (Jarvis et al., 2005; Xing et al., 2020). In this paper, a photometric dispersion analyzer (PDA) was used to study the coagulation kinetics and floc formation. In addition, scanning electron microscopy (SEM), X-ray diffraction (XRD) and Fourier transform infrared spectroscopy (FTIR) were employed to investigate the structure of flocs.

The results indicated that planar (sheet-like) flocs of lepidocrocite (γ-FeOOH), with large specific surface area, were formed, which were completely different from the flocs formed in the Fe(III) coagulation process; in addition, the growth of γ-FeOOH crystals was inhibited by the presence of HA, and independent of DO concentrations and pH. The experimental results obtained in this study are beneficial to understanding the Fe(II) coagulation and crystallization of flocs, and a possible mechanism for the formation of the crystalline planar flocs is proposed.

2. Materials and method

2.1 Materials

For the coagulation tests, a series of HA test solutions was prepared by adding various amounts of a HA stock solution (10 g/L) to 1 L deionized water which

contained 5 mM sodium bicarbonate ($NaHCO_3$), and which was then adjusted to specific initial pH values (7 or 9) with the addition of HCl or NaOH solution (0.2 M). The HA stock solution was prepared using the following method: 1 g humic acid sodium salt (H16752, Sigma Aldrich, USA) and 0.1 g NaOH were added to 100 mL deionized water and mixed with a magnetic stirrer for 24 h, as employed in the study of Yang and co-workers (Yang et al., 2020). Iron(II) sulfate ($FeSO_4$) and iron(III) sulfate ($Fe_2(SO_4)_3$) were used as coagulants with a concentration in the tests of 0.1 mM Fe(II)/(III). The HA (Sigma Aldrich) was technical grade and other reagents were analytical grade.

2.2 Experimental protocol

For the coagulation tests, the equipment used was a Flocculator (MY3000-2N, Wuhan Meiyu, China), which enables mixing speeds and times to be preset. The test solutions were prepared and either purged with high-purity nitrogen gas (0.1 L/h) for 0.5 h to remove oxygen, or aerated with an air flow (0.1 L/h) for 0.5 h to increase the initial DO concentration. When the application of nitrogen gas (N_2) or air into the solution was stopped, N_2 (0.2 L/h) was applied above the solution surface (about 0.5 cm) to prevent oxygen dissolving into the solution during coagulation. The initial pH of test solutions, before purged N_2 or air, was determined by pH meter (METTLER TOLEDO, Switzerland); the initial oxygen content of N_2 purged solutions (2 mg/L), and aerated solutions (6 mg/L), were measured by a dissolved oxygen apparatus (F4,

METTLER TOLEDO, Switzerland, with LE621 IP67 dissolved oxygen sensor). The coagulation experiments were conducted at room temperature (25±1 ºC). A 1 mL quantity of 0.1 M Fe(II)/(III) stock solution was added to the test solution (1000 mL) with rapid stirring. The stirring speed for rapid stirring was pre-set at 200 rpm for 1 min to give good mixing, and then reduced to 50 rpm for 30 min for flocs growth, followed by 200 rpm again for 1 min to break the flocs, and then back to 50 rpm for 20 min for flocs re-growth. During the coagulation process, samples corresponding to the formation, breakage and re-growth of flocs were continuously monitored by a Photometric Dispersion Analyzer (PDA2000, Rank Brothers Ltd, UK) based on the "turbidity fluctuation" technique. In this method, the Flocculation Index (FI) increases as flocs grow larger and details of the method are given elsewhere (Yu et al., 2011).

2.3 Characterization and analysis

Zeta potential was measured by a zeta sizer instrument (Nano ZS90, Malvern Inc., UK). In the coagulation test, once the FI reached a steady value during the first slow mixing period, samples of flocs were removed from solution, air-dried, gold-coated and analyzed by scanning electron microscope (SEM, Hitachi SU8020, Japan). Field emission transmission electron microscopy (TEM, JEM-2100F, JEOL, Japan) was used to analyze the crystallinity (lattice fringes). The nature of the flocs after they were freeze-dried was analyzed by Fourier Transform infrared spectroscopy (FTIR, NICOLET-8700, Thermo Fisher Scientific, America) and the absorption spectra were

obtained between 400 and 4,000 cm^{-1}. An X-ray diffractometer (XRD, X'Pert PRO MPD, PANalytical, Netherlands) was utilized to analyze the phase composition of the flocs at 40 kV and 40 mA, and at a scan speed of 4 ^{o}/min. X-ray photoelectron spectroscopy (XPS, PHI Quantera II, ULVAC, Japan) measurements were conducted with a Thermo Escalab 250 electron spectrometer using 150 W Al-Kα radiation and the binding energy was calibrated by C 1s (284.8 eV) (Luo et al., 2017).

3. Results and discussion

3.1 Coagulation process

As shown in Figure 1, there were significant differences in the coagulation processes and the structures of flocs between the Fe(II) and Fe(III) coagulants. When Fe(II) was used as the coagulant, the maximum FI value (size of flocs) was much greater and the lag time (from 0 s to the time when the FI value began to increase) was much longer than with Fe(III) as the coagulant (Figures 1a and 1b). The existence of the active oxygen-containing groups (-OH_2 and -OH) in the inner coordination spheres of the Fe ions, is the main cause of their tendency to attract each another through forming μ-OH bonds, and to form nanoparticles which aggregate to form flocs (Wu et al., 2019; Yu et al., 2016b). We believe that Fe(III) may have more active oxygen-containing groups (active points) than Fe(II) at the beginning, resulting in the formation of nanoparticles and flocs more rapidly than Fe(II). However, the surface of nanoparticles might become less active, or inactive, to re-aggregate if the

169 flocs are broken during the coagulation process, especially when the stirring rate
170 increased from 50 to 200 rpm, resulting in the size of flocs being smaller (Yu et al.,
171 2016b). Furthermore, the corresponding morphologies of the flocs, as observed by
172 scanning electron microscopy (SEM), were significantly different, with Fe(III) flocs
173 appearing as small sphere-like nanoparticles, while Fe(II) flocs morphologies were
174 large planar-like (Figures 1c-d); this is discussed in Section 3.5 in more detail. In
175 contrast to the small sphere-like nanoparticles, we believe that there are more active
176 points on the surface of large planar-like nanoparticles, and this leads to the formation
177 of larger flocs in Fe(II) coagulation, as shown in Figure 1a. The results of XRD
178 analysis demonstrated that the planar-like Fe(II) flocs were crystalline lepidocrocite
179 (γ-FeOOH) and the sphere-like Fe(III) flocs were amorphous $Fe(OH)_3$, which is
180 discussed in Section 3.3 in more detail. In addition, visual observation (Supporting
181 Information, Figure S1) indicated that the Fe(II) coagulation process proceeded in
182 three stages. In the first stage, quantities of green rust (a ferrous-ferric hydroxy salt)
183 were produced, and which then gradually turned into yellow Fe(III) compounds in the
184 second stage, as observed in previous research (Schwertmann et al., 1994). In the
185 third stage, slow stirring facilitated the aggregation of nanoparticles and the formation
186 of large flocs.

187 **Figure 1**

188

189 A series of experiments was carried out to investigate the effect of HA under

different DO concentrations and pH on the Fe(II) coagulation process. As shown in Figure 2a, the performance of Fe(II) coagulation was substantially affected by the concentration of HA at pH 7 and DO=2.0 mg/L. In particular, the lag time of Fe(II) aggregation decreased from approximately 870 s to 570 s and the maximum FI value after coagulation decreased from nearly 1.5% to 1.2%, when HA increased from 0 to 0.1 mg/L (Figure 2a). It was evident that the lag time of Fe(II) coagulation decreased until the concentration of HA exceeded 1 mg/L. In addition, the maximum FI values gradually decreased from nearly 1.2% to 1.1% when the HA concentration increased from 0.1 mg/L to 1 mg/L, and then declined markedly from nearly 1.1% to 0.8% when the HA concentration increased from 1 mg/L to 2 mg/L. When the HA concentration was ≥5 mg/L, the FI value maintained a low value (<0.2%) and the lag time was greater than 2500 s (Figures 2a and 2b). We believe that as the HA concentration increased, precipitates of Fe-HA complexes were more easily formed and able to come into close contact with each other; while at higher HA concentrations, an excess of HA covered the surface of nanoparticles and the presence of more steric repulsive forces prevented nanoparticle aggregation, as well as the effect of HA accelerating the Fe(II) oxidation rate (Jarvis et al., 2005; Jones et al., 2015). In addition, the presence of HA, especially at higher HA concentrations, decreased the zeta potential of flocs (Figure 3a), and it is suggested that the presence of electrostatic forces prevented aggregation of nanoparticles and the growth of flocs (Zhu et al., 2014).

In order to consider the effect of HA on the coagulation performance of Fe(II) under different DO concentrations, similar experiments were carried out with DO = 6.0 mg/L at pH 7. The results showed that the effect of HA, at different concentrations, on the coagulation rate of flocs under high DO conditions was similar to that under low DO conditions (Figure S2a). However, the variation of maximum FI values was different under high DO conditions. When the HA concentration was lower than 1.0 mg/L, the maximum FI values increased from 1.07% to 1.18%, which may be due to the bridging effect of HA, and they declined sharply when the HA concentration exceeded 2 mg/L under high DO conditions (Figure 2c); this may be due to the effect of electrostatic repulsion and steric hindrance of HA, as well as the effect of HA accelerating the Fe(II) oxidation rate (Jones et al., 2015; Zhu et al., 2014). It was found that under high DO concentrations (high Fe(II) oxidation rate), the Fe(II) coagulation behaviour with HA was more similar to that of the Fe(III) coagulation (Figure S2b). Compared to the effect of HA on the coagulation process at pH 7, the results at pH 9 were significantly different (Figures S2c-d). It was evident that under both low and high DO conditions, Fe(II) coagulation efficiency systematically decreased with increasing HA concentration from 0 to 2 mg/L, and at 2 mg/L no floc development was detected within 30 min (Figure 2d).

Figure 2

3.2 Characteristics of flocs during coagulation

The variation of zeta potential of Fe(II) flocs / precipitates during coagulation with different HA concentrations and pH was investigated in order to provide information concerning the development of charge on the particle surfaces. The zeta potential of samples formed with different HA concentrations was measured immediately after the samples were taken from the jar at different stirring times (0, 2, 5, 10, 15 and 20 min, respectively). Generally, the surface charge of (hydr)oxides was negative and oxidation time-dependent, such that the zeta potential decreased initially with the oxidation time and then remained constant with increasing time (Figures 3 and S3). As can be seen in Figure 3a, the zeta potential gradually decreased and eventually was almost the same as that of Fe(III) during the Fe(II) oxidation process at pH 7 and DO=2.0 mg/L. This indicated that the zeta potential of hydrolyzed Fe(III) species stabilized immediately, while some time was required for hydrolyzed Fe(II) species to be transformed to Fe(III) by dissolved oxygen. A large increase in the net negative charge was observed by raising pH from 7 to 9, which is due to the adsorption of hydroxyl ions (Hingston et al., 1967). Moreover, the zeta potential reached a stable value within 2 min at pH 9 as a result of the increasing oxidation rate of Fe(II) at higher pH (Morgan et al., 2007). As shown in Figures 3b and S3, the presence of an increasing HA concentration decreased the zeta potential, as well as the time before the zeta potential reached a stable value. The formation of Fe-HA complexes could lead to more carboxyl groups on the surface of Fe nanoparticles as HA concentration increased, thus causing a more negative potential complex (Jarvis et al., 2005); in

253 addition, the formation of Fe-HA complexes could also increase the oxidation rate of
254 Fe(II), thus shortening the time required for the zeta potential to reach a stable value
255 (Jones et al., 2015; Morgan et al., 2007). As the zeta potential for nanoparticles,
256 especially associated with HA, is far from 0 mV, this would weaken their aggregation
257 because of the electrostatic repulsion. However, the strength of the flocs or connection
258 efficiency of nanoparticles may be determined by the chemical bonds on the surface
259 of nanoparticles and the connection mechanism may not be charge neutralization (Yu
260 et al., 2016b).

261 Information concerning the functional groups on the surface of flocs during
262 coagulation was obtained by use of Fourier transform infrared (FTIR) spectroscopy.
263 Figure 3c gives some results showing the variation of functional groups during
264 coagulation with Fe(II) at pH 7 and DO=2.0 mg/L. Three samples were taken and
265 analyzed corresponding to when the solution colour turned to yellow at about 300 s,
266 when the flocs size just began to increase at about 800 s, and when the flocs size had
267 reached a steady state at about 2700 s. There were three peaks evident near 3177 cm^{-1},
268 2928 cm^{-1} and 2850 cm^{-1} on the spectrographs, corresponding to different hydroxyl
269 functional groups on the surface of flocs (Weckler et al., 1998). The absorption peaks
270 obtained at 1019 cm^{-1}, 886 cm^{-1} and 742 cm^{-1} corresponded to the different bending
271 vibrations of Fe-O-H, suggesting that the crystalline γ-FeOOH had formed when the
272 solution colour turned to yellow (Liu et al., 2013). It can be seen that with the increase
273 of stirring time from 300 s to 800 s, the strength of peaks corresponding to hydroxyl

groups and the chemical bonds Fe-O-H slightly decreased and increased, respectively. Our previous studies have shown that crystallization is a process of dehydration resulting in the decrease of active hydroxyl group (Wu et al., 2019). The subsequent slight decrease of peak intensity corresponding to Fe-O-H (2700 s) might be caused by the weakening of functional group activity when the nanoparticles aggregated or were broken during coagulation (Yu et al., 2010; Yu et al., 2016b).

Figure 3

3.3 Images of flocs after coagulation

The results of SEM images demonstrated that the presence of HA impeded the growth of planar-like flocs at pH 7 and DO=2.0 mg/L (Figures 4a-c). This result is similar to the finding that HA can hinder the crystallization process of aluminum flocs (Yu et al., 2018). In addition, the X-ray powder diffraction (XRD) patterns determined that planar-like flocs were γ-FeOOH with cell constants a = 3.87 Å, b = 12.51 Å, and c = 3.06 Å (JCPDS card 74-1877) (Figure 4f). It can be concluded from the XRD patterns that the presence of HA induced a decrease of the relative crystallinity of γ-FeOOH. It was also found that the formation of planar-like flocs in the absence of HA, and the effect of HA on the formation of γ-FeOOH, were independent of the DO concentration and pH (Figure S4a-f). In order to better understand the formation of crystalline planar-like flocs, a time-dependent experiment was carried out without HA at pH 7 and DO=2.0 mg/L to explore the formation

process of planar nanoparticles. Samples were collected when the solution colour appeared yellow (after about 300 s) during coagulation. It was found that the nanoparticles were already planar and crystalline in structure (Figures 4d and S4g) when the colour of solution became yellow. TEM images of flocs structures produced without HA at pH 7 and DO=2.0 mg/L are shown in Figure 4e. Particles after coagulation exhibited both a rod-shape (RL) and lath-shape (LL), which is in agreement with the findings of other researchers (Hansel et al., 2005; Kozin et al., 2014). The results of selected area electron diffraction (SAED) demonstrated that the substances are crystals of γ-FeOOH with exposed (002), (051), and (031) lattice planes (Figure 4e, inset). In contrast, the results of TEM, SAED and XRD demonstrated that the spherical-like substances were amorphous Fe(III)-(hydr)oxide ($Fe(OH)_3$ is widely used as the molecular formula) in the Fe(III) coagulation (Figure S4h-i).

Figure 4

3.4 Characteristics of flocs after coagulation

Further analysis of the composition of Fe(II) flocs formed at pH 7 and DO=2.0 mg/L was conducted through multiple characterization methods, including FTIR and high-resolution transmission electron microscopy (HR-TEM). These studies were undertaken to verify that the flocs were composed of γ-FeOOH. XRD analysis alone, was not able to reveal whether there were other Fe (hydr)oxides in the final floc

316 products, because the diffraction peaks of other Fe (hydr)oxides may overlap or
317 interfere with those of γ-FeOOH. From FTIR analysis of the sample formed without
318 HA at pH 7 and DO=2.0 mg/L, a trace of goethite (α-FeOOH) was detected as
319 revealed by the bands at 886 cm^{-1} which was assigned to in-plane Fe-O-H bending
320 vibrations of goethite (Figure 5a); this indicated that some γ-FeOOH might transform
321 into α-FeOOH during coagulation (Boland et al., 2014). The characteristic of Fe-O-H
322 bending vibration modes can be clearly seen at about 742 cm^{-1}, 1019 cm^{-1}, 1164 cm^{-1}
323 and 1339 cm^{-1}, confirming the formation of γ-FeOOH (Liu et al., 2013). The
324 absorption peak obtained at 1642 cm^{-1} was due to the vibration of H_2O in the crystal
325 structure (Yu et al., 2018), and the existence of the H–O–H bond confirmed the
326 FeOOH to be in hydrated form (Chen et al., 2014b). It was also observed that the
327 absorption peaks of HA increased as its concentration increased at 1375 cm^{-1} (COO-
328 symmetric stretch vibration) and 1577 cm^{-1} (C=C vibration) (Bian et al., 2011). The
329 presence of HA induced a decrease of the relative intensity of peaks for γ-FeOOH (at
330 742 $cm^{-1}$and 1019 cm^{-1}), which was consistent with the results of SEM and XRD
331 analyses. The peaks at about 1642 cm^{-1} and 1019 cm^{-1}, especially for the flocs formed
332 with 5 mg/L HA in solution, were affected by the –C=C (at 1704 cm^{-1}) and -C_6H_5
333 groups (at 1610 cm^{-1}), and -C-O groups (at 1030 cm^{-1} and 1089 cm^{-1}) of raw HA,
334 respectively (Pandey, 1999). In respect to the effect of HA, the results presented in
335 this work show that with increasing HA concentration, the crystallinity of Fe(II) flocs
336 decreased. Keeping nanoparticles within the effective distance of each other and

maintaining the surface activity of nanoparticles are important factors for crystal growth (ThomasArrigo et al., 2018; Zhu et al., 2018). In coagulation with HA, especially with high concentrations of HA, the surface active sites of nanoparticles were completely blocked, limiting atom adsorption onto the nanoparticles surface (Chen et al., 2014a), and the effect of electrostatic repulsion and the steric hindrance of HA prevented nanoparticle aggregation (Jarvis et al., 2005); thus, the γ-FeOOH growth was hindered.

In order to provide direct evidence of the existence of γ-FeOOH and goethite, the flocs after coagulation without HA at pH 7 with DO=2.0 mg/L were carefully investigated by using HR-TEM (Figure 5b-f). The resolved interplanar spacing of region A was 0.247 nm, which corresponds to the lattice planes (031) of γ-FeOOH and the angle between them coincided well with the γ-FeOOH unit cell structure (Figures 5c and 5e). The resolved interplanar spacings of region B were 0.419 nm, 0.270 nm and 0.170 nm, which corresponded to the (110), (130) and (240) lattice planes of α-FeOOH, respectively (Figure 5d). The calculated (110), (130) and (240) lattice planes and the angle between them coincided well with the goethite unit cell structure (Figure 5f).

X-ray photoelectron spectroscopy (XPS) is a versatile surface analysis technique that can be used for compositional and chemical state analysis. In order to study the surface and inner structure of the planar-like flocs formed without HA at pH 7 and DO=2.0 mg/L, XPS spectra of the surface and at a floc depth of 10 nm were obtained.

Figure 5g shows the full-survey-scan spectra at different depths of flocs which reveal the coexistence of Fe, O, and C elements in the sample. In addition, the Fe 3p peak position for Fe^{3+} was found to be 55.8 eV. The XPS spectrum of the Fe 2p region shows two major peaks located at 711.4 / 725.4 eV for Fe $2p_{3/2}$ / Fe $2p_{1/2}$, together with two shake-up satellites at 720.1 / 733.3 eV, which agreed well with values reported in the literature for FeOOH (Figure 5h) (Liu et al., 2016). It was found that the binding energies of Fe 2p decreased markedly to 709.8 / 723.0 eV for Fe $2p_{3/2}$ / Fe $2p_{1/2}$ at a depth of 10 nm. Fe 2p data on the surface of flocs are assigned to Fe^{3+} compounds, while within the structure of the flocs the Fe 2p data matched closely with Fe^{2+} compounds (Tan et al., 1990). This indicated that the Fe(II) on the surface of flocs transformed to Fe^{3+} after coagulation and oxidation, but did not change within the flocs.

Figure 5

3.5 The formation mechanism of planar-like γ-FeOOH

In this work, planar-like flocs were produced in Fe(II) coagulation and small spherical-like flocs were produced in Fe(III) coagulation. It was believed that the water and hydroxyl groups on the surface of precipitate particles could be released and form μ-OH bonds (Wu et al., 2019). Fe oxides and hydroxides are composed of different stacks of closely-packed oxygen/hydroxyl sheets, with various arrangements of the Fe ions in the interstices (Bernal et al., 1959); this leads to a difference in the

379 activity of the oxygen-containing groups around the Fe ions. We believe that the
380 surface oxygen-containing groups are all active so that the nanoparticles grow with
381 unrestricted orientation and form a spherical structure in the case of Fe(III)
382 coagulation. However, with Fe(II), it is possible that some surface oxygen-containing
383 groups are probably less active, which may be due to the different properties of
384 Fe-O-H bonds within Fe(II) hydroxides and Fe(III) hydroxides, so that the growth of
385 nanoparticles on some planes is inactive, thereby forming a planar-like morphology
386 (Figure 6a).

387 The results indicate that crystalline γ-FeOOH was produced in Fe(II) coagulation;
388 while amorphous $Fe(OH)_3$ was produced in Fe(III) coagulation. We believe that
389 γ-FeOOH was not formed from Fe(III) solution without the effect of high temperature
390 (Misawa et al., 1974). Based on the experimental results of XPS that Fe(II) existed
391 within the interior of nanoparticles (Figure 5h) and the low solubility of $Fe(OH)_2$
392 (about 10^{-6} M) at around neutral pH (Beverskog et al., 1996), it is concluded that
393 $Fe(OH)_2$ existed within the interior of γ-FeOOH and a plausible formation
394 mechanism is proposed. Firstly, the dosed Fe(II) ions are hydrolyzed and $Fe(OH)_2$
395 nanoparticles are formed rapidly due to the partial supersaturation of Fe compounds,
396 and then serve as nucleation centres for crystal growth. Subsequently, Fe(II) on the
397 surface of $Fe(OH)_2$ nanoparticles gradually changes to Fe(III) by oxidation.
398 Eventually, γ-FeOOH is formed when the solution colour turns completely yellow
399 (Figure 6b). The oxidation of $Fe(OH)_2$ within the interior of nanoparticles may be

impeded by the formation of γ-FeOOH on the surface of nanoparticles, which probably prevents the penetration of oxygen from the bulk solution (Sarin et al., 2004). It was speculated that the growth and polymerization process of γ-FeOOH may follow the 'Oriented attachment mechanism' (Zhu et al., 2018) instead of the 'Ostwald ripening mechanism' (Ostwald, 1897). This is because the Ostwald ripening mechanism involves the dissolution-reprecipitation of small nanoparticles which would cause the oxidation of Fe(II) in the interior of nanoparticles and it would be inconsistent with experimental results of XPS that Fe(II) existed within the interior of γ-FeOOH (Figure 5h). The differences between the crystal structures of Fe oxide or hydroxide are due to the different arrangements of Fe ions in the interstices between sheets of anions (Francombe, 1959). The crystal structures of $Fe(OH)_2$ and γ-FeOOH, are both layered and held together by hydrogen bonds with shared edges, which indicate that it is thermodynamically easy for $Fe(OH)_2$ to transform to γ-FeOOH (Figures S5a and S5b). It should be noted that $Fe(OH)_2$ is readily oxidized and its morphology is difficult to define and the mechanism still needs to be further explored.

Figure 6

4. Conclusions

In this study, the Fe(II) coagulation process and the structure of flocs, as well as the effect of HA, were studied and compared with Fe(III) coagulation. It was found that the coagulation processes of Fe(II) and Fe(III) coagulants were markedly different,

421 with a slower rate of floc formation, but a larger size of flocs formed, in the Fe(II)
422 coagulation than that in the Fe(III) coagulation. In addition, the presence of HA has a
423 major influence on the rate and magnitude of floc formation, and no floc development
424 was observed at high HA concentrations. It was also found that the structure of Fe(II)
425 and Fe(III) flocs was markedly different, with planar-like flocs formed in Fe(II)
426 coagulation and spherical-like flocs formed in Fe(III) coagulation. The results showed
427 that Fe(II) flocs were crystalline γ-FeOOH, and Fe(III) flocs was amorphous $Fe(OH)_3$;
428 the growth of γ-FeOOH was inhibited by the presence of HA, but independent of DO
429 concentration and pH. On the basis that Fe(II) existed within the structure of Fe(II)
430 flocs, we propose that the initial $Fe(OH)_2$ particles provide the nuclei for the epitaxial
431 growth of crystalline γ-FeOOH.
432

433 ## ■ AUTHOR INFORMATION

434 **Corresponding Author**

435 *Phone: 86-10-62910878; fax: 86-10-62910878; e-mail: liuting@bit.edu.cn
436 and wzyu@rcees.ac.cn.

437 **ORCID**

438 https://orcid.org/0000-0001-9776-8021

439 **Author Contributions**

440 Xian Li, Ting Liu and Wenzheng Yu design the experiments; Xian Li completed the
441 main experiments and wrote the draft; Mengjie Liu was involved in some experiments;

Nigel J. D. Graham, Wensheng Deng, Ting Liu and Wenzheng Yu made final revisions to this manuscript.

Acknowledgements

This work was financially supported by the Beijing Natural Science Foundation (8192042), Marie Curie International Incoming Fellowship (FP7-PEOPLE-2012-IIF-328867) within the 7th European Community Framework Programme, and Chinese Key Research and Development Plan of the Ministry of Science and Technology (2019YFD1100104 and 2019YFC1906501). The authors are grateful to the Experimental Center of Advanced Materials School of Materials Science & Engineering and Tinglu Song for the support in XPS characterization.

Appendix A. Supplementary data

The Supporting Information contains five Figures that complement the results summarized in the paper. These are: images showing changes of experimental phenomena during the Fe(II) coagulation process (Figure S1); the influence of HA on the coagulation kinetics of flocs under different conditions (Figure S2); the variation of zeta potential with oxidation time with different HA concentrations at pH 9 (Figure S3); SEM images, TEM images and XRD spectra of flocs formed under different conditions (Figure S4); crystal structures of $Fe(OH)_2$ and γ-FeOOH (Figure S5).

References

Bernal, J.;Dasgupta, D. and Mackay, A. (1959) The oxides and hydroxides of iron and their structural inter-relationships. Clay Minerals Bulletin 4(21), 15-30.

Beverskog, B. and Puigdomenech, I. (1996) Revised pourbaix diagrams for iron at 25–300 °C. 38(12), 0-2135.

Bian, S.W.;Mudunkotuwa, I.A.;Rupasinghe, T. and Grassian, V.H. (2011) Aggregation and dissolution of 4 nm ZnO nanoparticles in aqueous environments: influence of pH, ionic strength, size, and adsorption of humic acid. Langmuir 27(10), 6059-6068.

Boland, D.D.;Collins, R.N.;Miller, C.J.;Glover, C.J. and Waite, T.D. (2014) Effect of solution and solid-phase conditions on the Fe(II)-accelerated transformation of ferrihydrite to lepidocrocite and goethite. Environ Sci Technol 48(10), 5477-5485.

Chen, C.;Dynes, J.J.;Wang, J. and Sparks, D.L. (2014a) Properties of Fe-organic matter associations via coprecipitation versus adsorption. Environ Sci Technol 48(23), 13751-13759.

Chen, Y.C.;Lin, Y.G.;Hsu, Y.K.;Yen, S.C.;Chen, K.H. and Chen, L.C. (2014b) Novel iron oxyhydroxide lepidocrocite nanosheet as ultrahigh power density anode material for asymmetric supercapacitors. Small 10(18), 3803-3810.

Chorghe, D.;Sari, M.A. and Chellam, S. (2017) Boron removal from hydraulic fracturing wastewater by aluminum and iron coagulation: Mechanisms and limitations. Water Research 126, 481-487.

Cornell, R.M. and Schwertmann, U. (2003) The iron oxydes: structure, Properties, Reactions, Occurences and Uses, Wiley-VCH.

De Yoreo, J.J.;Gilbert, P.U.;Sommerdijk, N.A.;Penn, R.L.;Whitelam, S.;Joester, D.;Zhang, H.;Rimer, J.D.;Navrotsky, A. and Banfield, J.F. (2015) Crystallization by particle attachment in synthetic, biogenic, and geologic environments. Science 349(6247), aaa6760.

Duan, J. and Gregory, J. (2003) Coagulation by hydrolysing metal salts. Advances in Colloid and Interface Science 100-102, 475-502.

Ellis, W.C.;McDaniel, N.D.;Bernhard, S. and Collins, T.J. (2010) Fast water oxidation using iron. Journal of the American Chemical Society 132(32), 10990-10991.

Francombe, M.H. (1959) Structure Transformations Effected by the Dehydration of Diaspore, Goethite and Delta Ferric Oxide. Clay Minerals 4(21), 1-14.

Gaffney, J.W.;White, K.N. and Boult, S. (2008) Oxidation state and size of Fe controlled by organic matter in natural waters. Environmental Science & Technology 42(10), 3575-3581.

Hansel, C.M.;Benner, S.G. and Fendorf, S. (2005) Competing Fe (II)-induced mineralization pathways of ferrihydrite. Environmental Science & Technology 39(18), 7147-7153.

Hingston, F.J.;Atkinson, R.J.;Posner, A.M. and Quirk, J.P. (1967) Specific Adsorption of Anions. Nature 215(5109), 1459-1461.

505 Hsu, P.H. (1976) Comparison of iron(III) and aluminum in precipitation of phosphate
506 from solution. Water Research 10(10), 903-907.
507 Hu, J.-S.;Zhong, L.-S.;Song, W.-G. and Wan, L.-J. (2008) Synthesis of Hierarchically
508 Structured Metal Oxides and their Application in Heavy Metal Ion Removal.
509 Advanced Materials 20(15), 2977-2982.
510 Jarvis, P.;Jefferson, B. and Parsons, S.A. (2005) How the Natural Organic Matter to
511 Coagulant Ratio Impacts on Floc Structural Properties. Environmental Science and
512 Technology 39(22), 8919-8924.
513 Jones, A.M.;Griffin, P.J. and Waite, T.D. (2015) Ferrous iron oxidation by molecular
514 oxygen under acidic conditions: The effect of citrate, EDTA and fulvic acid.
515 Geochimica et Cosmochimica Acta 160, 117-131.
516 Kozin, P.A.;Salazar-Alvarez, G. and Boily, J.F. (2014) Oriented aggregation of
517 lepidocrocite and impact on surface charge development. Langmuir 30(30),
518 9017-9021.
519 Liu, B.;Qu, F.;Chen, W.;Liang, H.;Wang, T.;Cheng, X.;Yu, H.;Li, G. and Van der
520 Bruggen, B. (2017) Microcystis aeruginosa-laden water treatment using enhanced
521 coagulation by persulfate/Fe(II), ozone and permanganate: Comparison of the
522 simultaneous and successive oxidant dosing strategy. Water Res 125, 72-80.
523 Liu, B.;Qu, F.;Yu, H.;Tian, J.;Chen, W.;Liang, H.;Li, G. and Van der Bruggen, B.
524 (2018) Membrane Fouling and Rejection of Organics during Algae-Laden Water
525 Treatment Using Ultrafiltration: A Comparison between in Situ Pretreatment with

526 Fe(II)/Persulfate and Ozone. Environ Sci Technol 52(2), 765-774.
527 Liu, J.;Zheng, M.;Shi, X.;Zeng, H. and Xia, H. (2016) Amorphous FeOOH Quantum
528 Dots Assembled Mesoporous Film Anchored on Graphene Nanosheets with Superior
529 Electrochemical Performance for Supercapacitors. Advanced Functional Materials
530 26(6), 919-930.
531 Liu, L.;Yang, L.-Q.;Liang, H.-W.;Cong, H.-P.;Jiang, J. and Yu, S.-H. (2013)
532 Bio-inspired fabrication of hierarchical feooh nanostructure array films at the air–
533 water interface, their hydrophobicity and application for water treatment. ACS Nano
534 7(2), 1368-1378.
535 Luo, W.;Jiang, C.;Li, Y.;Shevlin, S.A.;Han, X.;Qiu, K.;Cheng, Y.;Guo, Z.;Huang, W.
536 and Tang, J. (2017) Highly crystallized α-FeOOH for a stable and efficient oxygen
537 evolution reaction. Journal of Materials Chemistry A 5(5), 2021-2028.
538 Ma, M.;Liu, R.;Liu, H. and Qu, J. (2012) Effect of moderate pre-oxidation on the
539 removal of Microcystis aeruginosa by KMnO4-Fe(II) process: significance of the
540 in-situ formed Fe(III). Water Res 46(1), 73-81.
541 Matamoros-Veloza, A.;Cespedes, O.;Johnson, B.R.G.;Stawski, T.M.;Terranova, U.;de
542 Leeuw, N.H. and Benning, L.G. (2018) A highly reactive precursor in the iron sulfide
543 system. Nat Commun 9(1), 3125.
544 Meng, F.;Morin, S.A. and Jin, S. (2011) Rational solution growth of alpha-FeOOH
545 nanowires driven by screw dislocations and their conversion to alpha-Fe2O3
546 nanowires. J Am Chem Soc 133(22), 8408-8411.

547 Misawa, T.;Hashimoto, K. and Shimodaira, S. (1974) The mechanism of formation of
548 iron oxide and oxyhydroxides in aqueous solutions at room temperature. Corrosion
549 Science 14(2), 131-149.
550 Morgan, B. and Lahav, O. (2007) The effect of pH on the kinetics of spontaneous
551 Fe(II) oxidation by O2 in aqueous solution--basic principles and a simple heuristic
552 description. Chemosphere 68(11), 2080-2084.
553 Okamura, M.;Kondo, M.;Kuga, R.;Kurashige, Y.;Yanai, T.;Hayami, S.;Praneeth,
554 V.K.;Yoshida, M.;Yoneda, K.;Kawata, S. and Masaoka, S. (2016) A pentanuclear
555 iron catalyst designed for water oxidation. Nature 530(7591), 465-468.
556 Ostwald, W. (1897) Studien über die Bildung und Umwandlung fester Körper.
557 Zeitschrift für physikalische Chemie 22(1), 289-330.
558 Pandey, K. (1999) A study of chemical structure of soft and hardwood and wood
559 polymers by FTIR spectroscopy. Journal of Applied Polymer Science 71(12),
560 1969-1975.
561 Sarin, P.;Snoeyink, V.;Lytle, D. and Kriven, W. (2004) Iron corrosion scales: model
562 for scale growth, iron release, and colored water formation. Journal of Environmental
563 Engineering 130(4), 364-373.
564 Sayed, F.N. and Polshettiwar, V. (2015) Facile and sustainable synthesis of shaped
565 iron oxide nanoparticles: effect of iron precursor salts on the shapes of iron oxides.
566 Sci Rep 5, 9733.
567 Schwertmann, U. and Fechter, H. (1994) The formation of green rust and its

568 transformation to lepidocrocite. Clay Minerals 29(1), 87-92.
569 Shekhah, O.;Ranke, W.;Schule, A.;Kolios, G. and Schlogl, R. (2003) Styrene
570 synthesis: high conversion over unpromoted iron oxide catalysts under practical
571 working conditions. Angew Chem Int Ed Engl 42(46), 5760-5763.
572 Shu, Z.;Liu, L.;Tan, W.;Suib, S.L.;Qiu, G.;Yang, X.;Zheng, L. and Liu, F. (2019)
573 Solar Irradiation Induced Transformation of Ferrihydrite in the Presence of Aqueous
574 Fe(2). Environ Sci Technol 53(15), 8854-8861.
575 Su, Z.;Liu, T.;Yu, W.;Li, X. and Graham, N.J.D. (2017) Coagulation of surface water:
576 Observations on the significance of biopolymers. Water Res 126, 144-152.
577 Tagliabue, A.;Bowie, A.R.;Boyd, P.W.;Buck, K.N.;Johnson, K.S. and Saito, M.A.
578 (2017) The integral role of iron in ocean biogeochemistry. Nature 543(7643), 51-59.
579 Tan, B.J.;Klabunde, K.J. and Sherwood, P.M. (1990) X-ray photoelectron
580 spectroscopy studies of solvated metal atom dispersed catalysts. Monometallic iron
581 and bimetallic iron-cobalt particles on alumina. Chemistry of Materials 2(2), 186-191.
582 ThomasArrigo, L.K.;Byrne, J.M.;Kappler, A. and Kretzschmar, R. (2018) Impact of
583 Organic Matter on Iron(II)-Catalyzed Mineral Transformations in
584 Ferrihydrite-Organic Matter Coprecipitates. Environ Sci Technol 52(21),
585 12316-12326.
586 Weckler, B. and Lutz, H.D. (1998) Lattice vibration spectra. Part XCV. Infrared
587 spectroscopic studies on the iron oxide hydroxides goethite (α), akaganéite (β),
588 lepidocrocite (γ), and feroxyhite (δ). European Journal of Solid State & Inorganic

589 Chemistry 35(8-9), 531-544.
590 Wu, M.;Yu, W.;Qu, J. and Gregory, J. (2019) The variation of flocs activity during
591 floc breakage and aging, adsorbing phosphate, humic acid and clay particles. Water
592 Res 155, 131-141.
593 Xing, B.;Graham, N. and Yu, W. (2020) Transformation of siderite to goethite by
594 humic acid in the natural environment. Communications Chemistry 3(1).
595 Xu, W.;Gao, B.;Yue, Q. and Wang, Y. (2010) Effect of shear force and solution pH
596 on flocs breakage and re-growth formed by nano-Al(13) polymer. Water Res 44(6),
597 1893-1899.
598 Yang, H.;Wu, X.;Su, L.;Ma, Y.;Graham, N.J.D. and Yu, W. (2020) The Fe-N-C
599 oxidase-like nanozyme used for catalytic oxidation of NOM in surface water. Water
600 Res 171, 115491.
601 Yang, H.G. and Zeng, H.C. (2004) Creation of intestine-like interior space for
602 metal-oxide nanostructures with a quasi-reverse emulsion. Angew Chem Int Ed Engl
603 43(39), 5206-5209.
604 Yang, Y.;Wang, S.;Xu, Y.;Zheng, B. and Liu, J. (2016) Molecular-Scale Study of
605 Aspartate Adsorption on Goethite and Competition with Phosphate. Environ Sci
606 Technol 50(6), 2938-2945.
607 Yu, W.-Z.;Gregory, J. and Campos, L. (2010) Breakage and regrowth of Al-humic
608 flocs-effect of additional coagulant dosage. Environmental Science & Technology
609 44(16), 6371-6376.

610 Yu, W.;Graham, N.J. and Fowler, G.D. (2016a) Coagulation and oxidation for
611 controlling ultrafiltration membrane fouling in drinking water treatment: Application
612 of ozone at low dose in submerged membrane tank. Water Res 95, 1-10.
613 Yu, W.;Gregory, J. and Campos, L.C. (2011) Breakage and re-growth of flocs: effect
614 of additional doses of coagulant species. Water Res 45(20), 6718-6724.
615 Yu, W.;Gregory, J.;Campos, L.C. and Graham, N. (2015) Dependence of floc
616 properties on coagulant type, dosing mode and nature of particles. Water Res 68,
617 119-126.
618 Yu, W.;Xu, L.;Lei, K. and Gregory, J. (2018) Effect of crystallization of settled
619 aluminum hydroxide precipitate on "dissolved Al". Water Res 143, 346-354.
620 Yu, W.Z.;Gregory, J. and Graham, N. (2016b) Regrowth of Broken Hydroxide Flocs:
621 Effect of Added Fluoride. Environ Sci Technol 50(4), 1828-1833.
622 Zhang, D.;Wang, Y.;Gao, H.;Fan, X.;Guo, Y.;Wang, H. and Zheng, H. (2019)
623 Variations in macro and micro physicochemical properties of activated sludge under a
624 moderate oxidation-in situ coagulation conditioning: Relationship between molecular
625 structure and dewaterability. Water Res 155, 245-254.
626 Zhang, X.;Shen, Z.;Liu, J.;Kerisit, S.N.;Bowden, M.E.;Sushko, M.L.;De Yoreo, J.J.
627 and Rosso, K.M. (2017) Direction-specific interaction forces underlying zinc oxide
628 crystal growth by oriented attachment. Nat Commun 8(1), 835.
629 Zhong, L.S.;Hu, J.S.;Liang, H.P.;Cao, A.M.;Song, W.G. and Wan, L.J. (2006)
630 Self-Assembled 3D Flowerlike Iron Oxide Nanostructures and Their Application in

Water Treatment. Advanced Materials 18(18), 2426-2431.

Zhou, J.;Liu, J.;Zhao, Z.;Peng, W.;Cui, F. and Liang, Z. (2019) Microcystis aeruginosa-laden water treatment using peroxymonosulfate enhanced Fe (II) coagulation: Performance and the role of in situ formed Fe3O4. Chemical Engineering Journal, 123012.

Zhu, C.;Liang, S.;Song, E.;Zhou, Y.;Wang, W.;Shan, F.;Shi, Y.;Hao, C.;Yin, K.;Zhang, T.;Liu, J.;Zheng, H. and Sun, L. (2018) In-situ liquid cell transmission electron microscopy investigation on oriented attachment of gold nanoparticles. Nat Commun 9(1), 421.

Zhu, M.;Wang, H.;Keller, A.A.;Wang, T. and Li, F. (2014) The effect of humic acid on the aggregation of titanium dioxide nanoparticles under different pH and ionic strengths. Sci Total Environ 487, 375-380.

- **Figure captions**

- Figure 1. Effect of coagulant type on the growth of flocs at pH 7 (a and b); SEM images of Fe(II) flocs formed at pH 7 (c) and Fe(III) flocs (d) (The dosage of coagulant was 0.1 M Fe(II)/Fe(III); scale bar: 100 nm).

- Figure 2. Effect of HA concentration on the growth of flocs at pH 7 and DO=2.0

652 mg/L (a and b, HA was added before Fe(II) addition); Effect of HA on the size of
653 flocs with different DO concentrations at pH 7 (c) and pH 9 (d).
654
655 ■ Figure 3. The variation of zeta potential of $FeSO_4$ / $Fe_2(SO_4)_3$ coagulants (0.1
656 mM) at pH 7/9 and DO=2.0 mg/L (a); Effect of HA concentration on the zeta
657 potential of $FeSO_4$ coagulants (0.1 mM) at pH 7 and DO=2.0 mg/L (b); FTIR
658 spectra of samples at different times during coagulation when using $FeSO_4$ (0.1
659 mM) as coagulant at pH 7 and DO=2.0 mg/L (c).
660
661 ■ Figure 4. SEM images of flocs formed at pH 7 and DO=2.0 mg/L with different
662 HA concentrations in bulk solution: (a) HA=0 mg/L, (b) HA=1 mg/L, (c) HA=5
663 mg/L, (d) SEM images of initial flocs (about 300 s) without HA; (e) TEM images
664 of flocs formed at pH 7 and DO=2.0 mg/L without HA and SAED images of
665 lepidocrocite (Inset); (f) XRD spectra of flocs formed at pH 7 and DO=2.0 mg/L
666 with different HA concentrations (Scale bar on SEM images are 100 nm).
667
668 ■ Figure 5. FTIR spectra of flocs after coagulation at pH 7 and DO=2.0 mg/L with
669 different HA concentrations (a); representative TEM images (b) and HRTEM
670 images of lepidocrocite (c) and goethite (d); schematic diagram of goethite and
671 lepidocrocite unit cell structure (e and f) drawn by Diamond 3.2 software (Crystal
672 Impact GbR, Germany); The survey and high-resolution scans of XPS spectra:

673 Total survey scans (g) and Fe 2p peaks of flocs (h). TEM, HR-TEM and XPS
674 samples were taken after coagulation at pH 7 and DO=2.0 mg/L with HA=0 mg/L
675 (scale bar on TEM and HR-TEM images are 100 nm and 5 nm, respectively).
676
677 ■ Figure 6. Schematics of Fe(II) & Fe(III) coagulation (a), and representation of the
678 pathway for the γ-FeOOH epitaxial growth from the initial $Fe(OH)_2$ suspensions
679 (b).
680

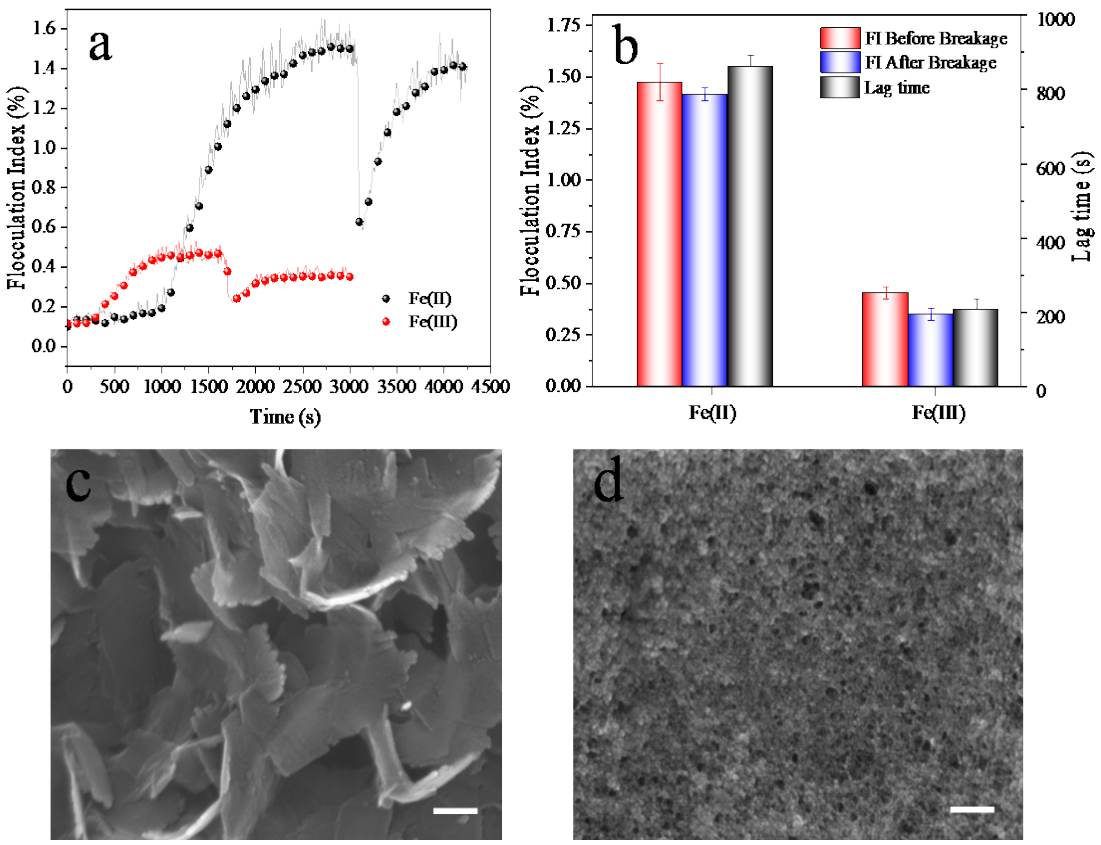


Figure 1. Effect of coagulant type on the growth of flocs at pH 7 (a and b); SEM images of flocs formed at pH 7 : Fe(II) flocs (c) and Fe(III) flocs (d). (The dosage of coagulant was 0.1 mM Fe(II)/Fe(III); scale bar: 100 nm).

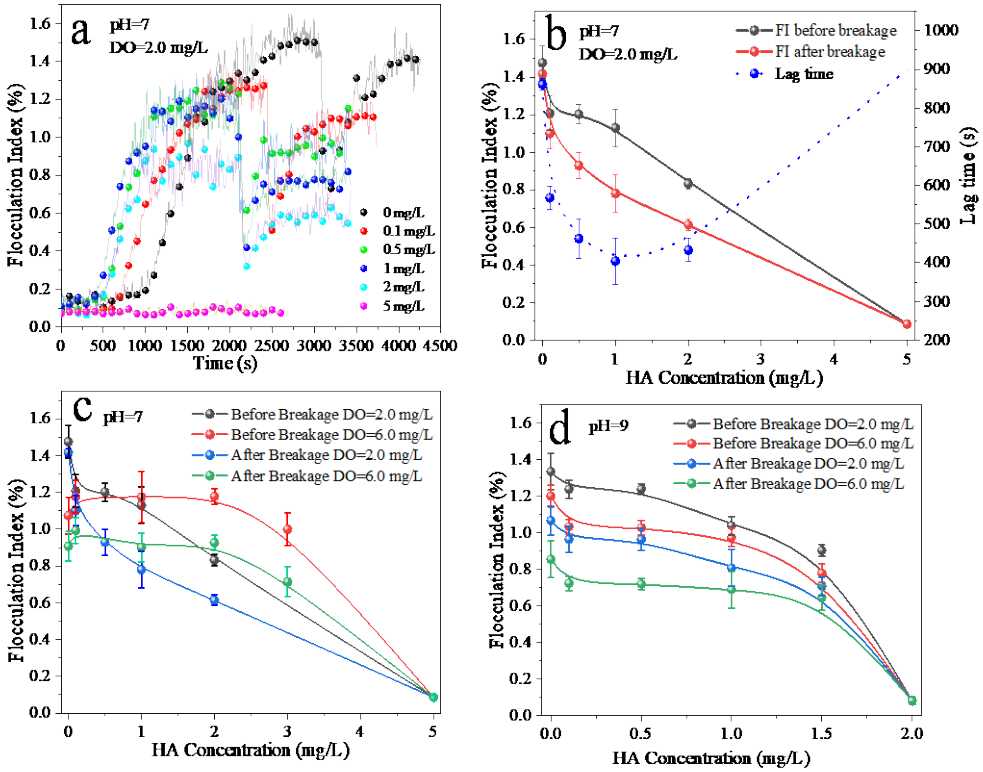


Figure 2. Effect of HA concentration on the growth of flocs at pH 7 and DO=2.0 mg/L (a and b, HA was added before Fe(II) addition); Effect of HA and DO concentrations on the size of flocs at pH 7 (c) and pH 9 (d).

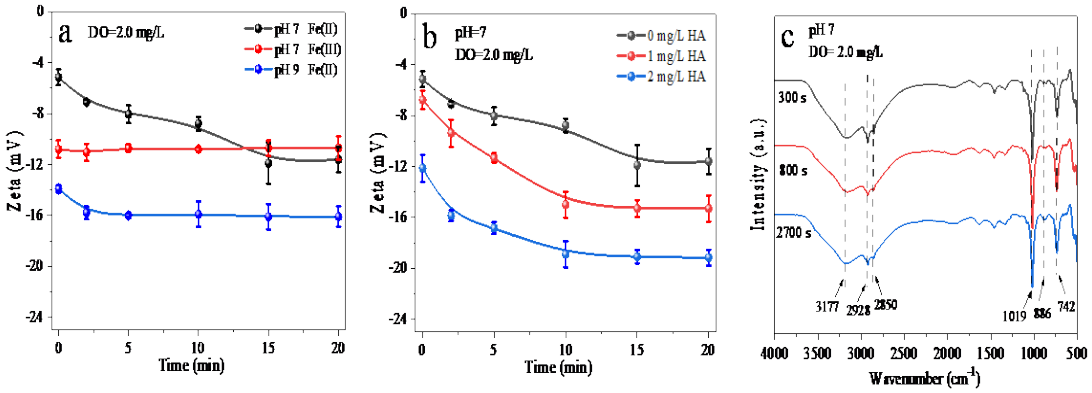


Figure 3. The variation of zeta potential of $FeSO_4$ / $Fe_2(SO_4)_3$ coagulants (0.1 mM) at pH 7/9 and DO=2.0 mg/L (a); Effect of HA concentration on the zeta potential of $FeSO_4$ coagulants (0.1 mM) at pH 7 and DO=2.0 mg/L (b); FTIR spectra of samples at different times during coagulation when using $FeSO_4$ (0.1 mM) as coagulant at pH 7 and DO=2.0 mg/L (c).

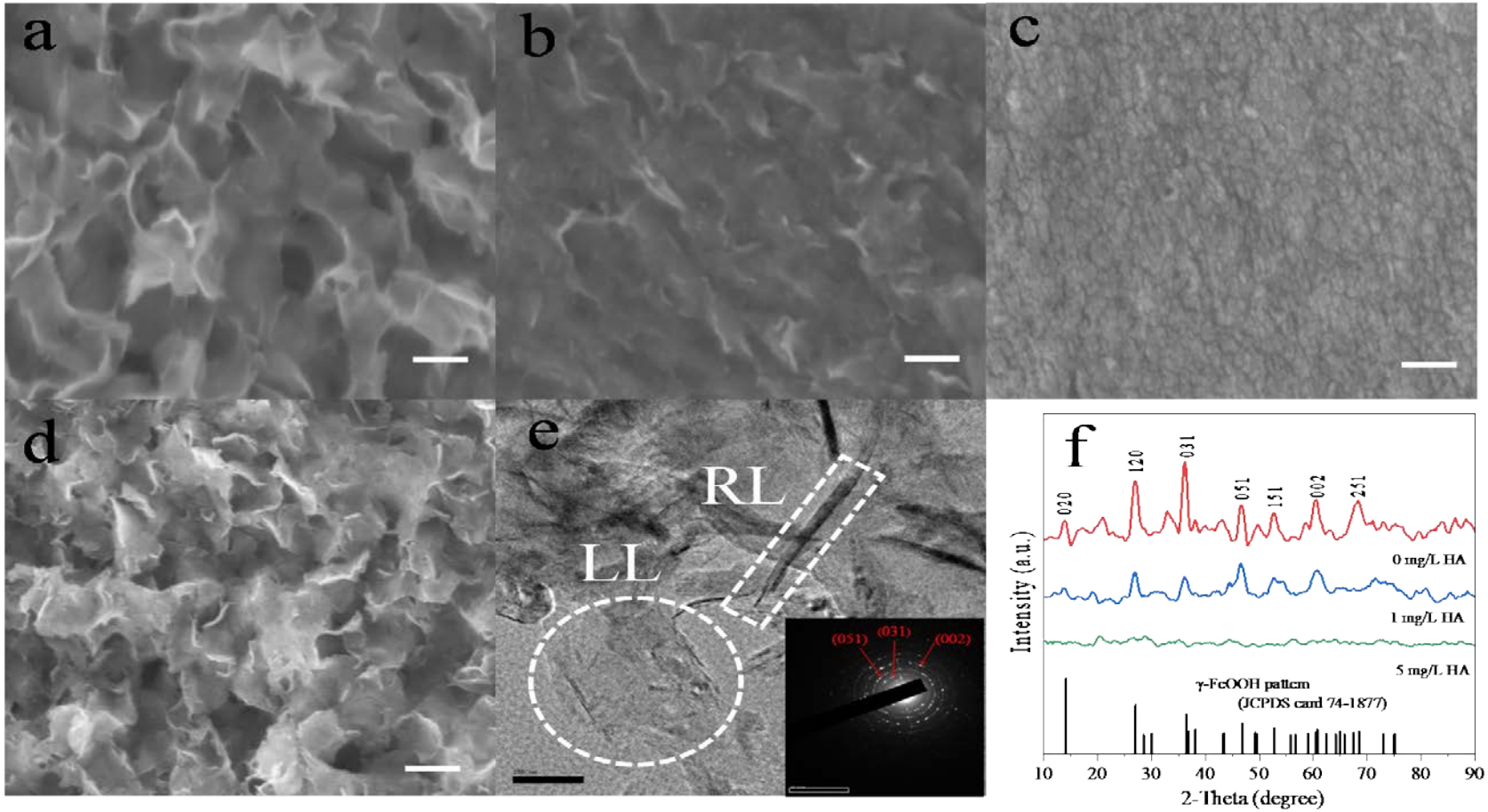


Figure 4. SEM images of flocs formed at pH 7 and DO=2.0 mg/L with different HA concentrations in bulk solution: (a) HA=0 mg/L, (b) HA=1 mg/L, (c) HA=5 mg/L, (d) SEM images of initial flocs (about 300 s) without HA; (e) TEM images of flocs formed at pH 7 and DO=2.0 mg/L without HA and SAED images of lepidocrocite (Inset); (f) XRD spectra of flocs formed at pH 7 and DO=2.0 mg/L with different HA concentrations (Scale bar on SEM images are 100 nm).

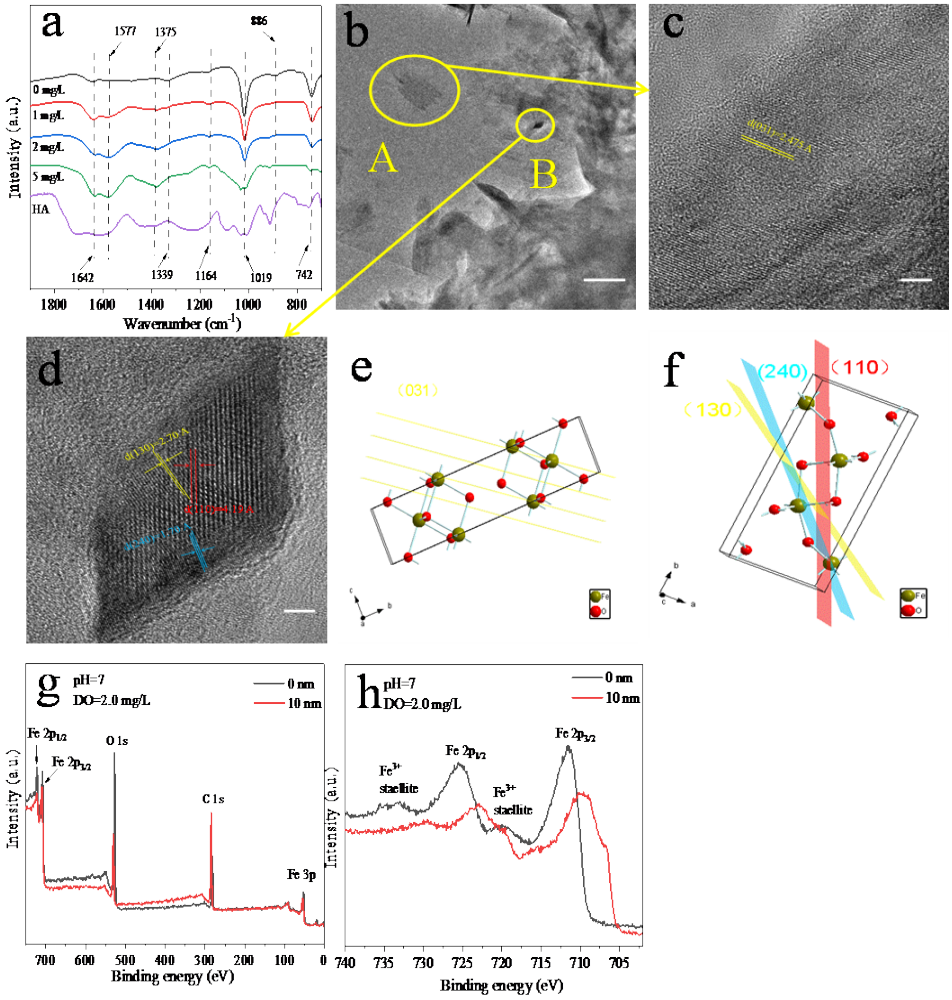


Figure 5. FTIR spectra of flocs after coagulation at pH 7 and DO=2.0 mg/L with different HA concentrations (a); representative TEM images (b) and HRTEM images of lepidocrocite (c) and goethite (d); schematic diagram of goethite and lepidocrocite unit cell structure (e and f) drawn by Diamond 3.2 software (Crystal Impact GbR, Germany); The survey and high-resolution scans of XPS spectra: Total survey scans (g) and Fe 2p peaks of flocs (h). TEM, HR-TEM and XPS samples were taken after coagulation at pH 7 and DO=2.0 mg/L with HA=0 mg/L (scale bar on TEM and HR-TEM images are 100 nm and 5 nm, respectively).

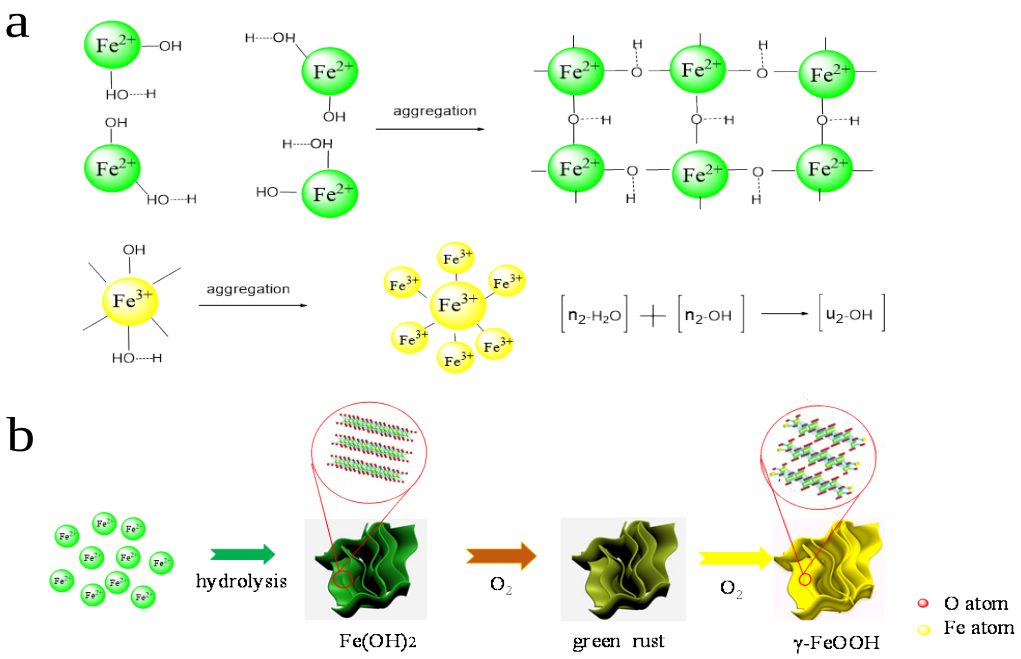


Figure 6. Schematics of Fe(II) & Fe(III) coagulation (a), and representation of the pathway for the γ-FeOOH epitaxial growth from the initial $Fe(OH)_2$ suspensions (b).